

## ORIGINAL ARTICLE

# Thermoelectric performance enhancement in *n*-type Bi<sub>2</sub>(TeSe)<sub>3</sub> alloys owing to nanoscale inhomogeneity combined with a spark plasma-textured microstructure

Yu Pan and Jing-Feng Li

Bi<sub>2</sub>Te<sub>3</sub> is a good thermoelectric compound that can be adjusted to *p*- or *n*-type with corresponding substitutions; however, less progress has been achieved for the property enhancement of *n*-type Bi<sub>2</sub>(TeSe)<sub>3</sub> compared with *p*-type (BiSb)<sub>2</sub>Te<sub>3</sub>. Textured *n*-type Bi<sub>2</sub>(TeSe)<sub>3</sub> with an enhanced thermoelectric performance has been developed in this study by combining texturing with *in situ* nanostructuring effects. The spark plasma-textured structure boosts the electrical transport properties and the power factors as benefits of the layered microstructure. It also leads to a simultaneous rise in the thermal conductivity along the *a*-axis. We developed a method to suppress increases in the thermal conductivity by inducing nanostructures, such as highly distorted regions and nanoscopic defect clusters, as well as dislocation loops that can form when texturing occurs at an optimized temperature. In this work, textured *n*-type Bi<sub>2</sub>(TeSe)<sub>3</sub> materials having enhanced thermoelectric performances within a low temperature range are developed with a maximum dimensionless figure of merit ( $ZT_{\max}$ ) exceeding 1.1 at 473 K. The present method, which synergetically utilizes the texturing and nanostructuring effects, could also be applied to other thermoelectric compounds having layered structures.

NPG Asia Materials (2016) 8, e275; doi:10.1038/am.2016.67; published online 3 June 2016

## INTRODUCTION

Thermoelectric materials that can be used for converting waste heat into electrical energy and for cooling in solid-state applications have attracted worldwide interest for decades.<sup>1–4</sup> The thermoelectric conversion efficiency of a material depends on its dimensionless figure of merit  $ZT$ , defined as  $ZT = \alpha^2 \sigma T / \kappa$ , where  $\alpha$ ,  $\sigma$ ,  $\kappa$  and  $T$  are the Seebeck coefficient, electrical conductivity, thermal conductivity and absolute temperature, respectively.<sup>5,6</sup> A great variety of thermoelectric materials have been developed and thoroughly studied,<sup>7–9</sup> but industrial applications are still dominated by bismuth telluride (Bi<sub>2</sub>Te<sub>3</sub>)-based alloys.<sup>10</sup> Therefore, extensive studies have been devoted to the enhancement of their properties. Industrially used ingots of Bi<sub>2</sub>Te<sub>3</sub>-based alloys are fabricated using a zone melting process, which is capable of enhancing the preferential crystal growth and chemical purity. Recent studies have demonstrated that property enhancements can be achieved with powder processes that facilitate nanostructuring and microstructure refinement, especially in *p*-type (BiSb)<sub>2</sub>Te<sub>3</sub> alloys.<sup>11–13</sup> In addition, powder-processed thermoelectric materials also possess better mechanical properties, which are beneficial in device manufacturing.<sup>14,15</sup> In particular, spark plasma sintering (SPS) combined with mechanical alloying (MA) has been increasingly used as a facile powder process for synthesizing thermoelectric materials.<sup>16–19</sup> Nevertheless, for the  $ZT$  enhancement of Bi<sub>2</sub>Te<sub>3</sub>-based alloys fabricated by MA and SPS, the optimal composition needs to be

redefined; it is no longer the same as the ingots because of massive point defects and strong donor-like effect.<sup>19,20</sup> Our group has already confirmed that Bi<sub>2</sub>Te<sub>2.2</sub>Se<sub>0.8</sub> is the optimal composition for samples prepared by MA and SPS.<sup>21</sup>

Bi<sub>2</sub>Te<sub>3</sub> is anisotropic with a layered structure composed of a quintuple atomic series in the order of Te(1)-Bi-Te(2)-Bi-Te(1) along the *c*-axis. Their electrical and thermal conductivities along the *a*-axis (in the *c*-plane) are approximately four and two times higher, respectively, than those along the *c*-axis of Bi<sub>2</sub>Te<sub>3</sub>.<sup>22,23</sup> However, the Seebeck coefficient is less dependent on the crystallography.<sup>24</sup> As a result, the  $ZT$  value in the *c*-plane is approximately two times higher than that perpendicular to the *c*-plane. Therefore, an improved  $ZT$  value can be expected when utilizing the anisotropic electrical and thermal transport properties,<sup>25</sup> especially for *n*-type Bi<sub>2</sub>(TeSe)<sub>3</sub>, which has a larger ratio of the electrical conductivities along the *a*- and *c*-axes than that of thermal conductivities. However, the electrical transport properties do not improve as much as expected by texturing because of the many complex chemical defect reactions induced mechanically during the texturing process. Therefore, it is important to suppress a rise in the thermal conductivity by incorporating nanostructures into the textured microstructures, as demonstrated in this study.

This work revealed the importance of synergetically combined texturing and nanostructuring effects that are realized by simply optimizing the texturing temperature. In this work, highly textured

*n*-type Bi<sub>2</sub>(TeSe)<sub>3</sub> alloys were fabricated by a repeated SPS process as hot-forging,<sup>26,27</sup> and a thermoelectric property enhancement was achieved by optimizing the texturing temperatures. A maximum *ZT* value of 1.1 was obtained in textured *n*-type Bi<sub>2</sub>Te<sub>2.2</sub>Se<sub>0.8</sub> (approximately 35% enhancement compared with the non-textured counterparts). A bottleneck has existed for the enhancement of *n*-type Bi<sub>2</sub>(TeSe)<sub>3</sub> alloys, and high *ZT*s exceeding 1.0 have been seldom reported in powder-processed *n*-type Bi<sub>2</sub>(TeSe)<sub>3</sub> despite higher *ZT* values demonstrated for *p*-type (BiSb)<sub>2</sub>Te<sub>3</sub> alloys.<sup>19</sup> We have demonstrated that a large quantity of nanoscopic defects inside the grains form at an optimized texturing temperature, decreasing the lattice thermal conductivity; meanwhile, a textured structure greatly enhances the electrical transport properties.

## EXPERIMENTAL PROCEDURES

### Materials synthesis

Mixtures of Bi (99.99%), Te (99.999%) and Se (99.999%) powders were subjected to MA in a planetary ball mill at 450 r.p.m. for 3 h, with a stoichiometric proportion of Bi<sub>2</sub>Te<sub>2.2</sub>Se<sub>0.8</sub>. The mill vials were filled with 95 vol. % Ar and 5 vol. % H<sub>2</sub> to provide a protective atmosphere. The mechanically alloyed powders were sintered by SPS in a Φ12-mm graphite mold at 673 K for 5 min under an axial pressure of 50 MPa in vacuum. Then the sintered samples were set into bigger molds with diameters from Φ15 to Φ20 mm and pressed also by SPS under a pressure of 50 MPa at different temperatures; the samples were named TP 400, TP 460, TP 480 and TP 500, respectively, for the temperatures of 673, 733, 753 and 773 K. The TP 460 sample was further texture-processed an additional time by SPS at 733 K in a Φ25-mm mold and named TP 460-3.

### Phase identification and microstructure characterization

Phase and textured structures were investigated by X-ray diffraction (XRD, D/max-RB, Rigaku, Tokyo, Japan) using Cu-Kα radiation ( $\lambda = 1.5406 \text{ \AA}$ ). The microstructures and nanostructures of the bulk samples were observed by field emission scanning electron microscopy (SEM, JSM-7001, JEOL, Tokyo, Japan) and transmission electron microscopy (TEM, JEOL-2011). The specimens used for the TEM observation were polished to ~30–40 μm and then thinned to electron transparency using a Leica precession ion-milling system (RES101, Bal-Tec, Pfäffikon, Switzerland) at a low angle (10–15°). High-resolution TEM (HRTEM) images of the pieces were recorded at 200 kV.

### Thermoelectric transport property measurement

The electrical resistivity and Seebeck coefficient were measured on a ZEM-2 apparatus (Ulvac-Riko, Yokohama, Japan) from 323 to 573 K in a helium atmosphere using a four-probe method. The Hall coefficient ( $R_H$ ) was measured using a Hall measurement system (ResiTest 8340DC, Tokyo, Japan), and the Hall carrier concentration ( $n_H$ ) and mobility ( $\mu_H$ ) were calculated by

$n_H = 1/(eR_H)$  and  $\mu_H = R_H/\rho$  in which  $\rho$  is electrical resistivity. The thermal diffusivity ( $D$ ) was measured using the laser flash method (TC-9000, Ulvac-Riko) in vacuum at temperatures ranging from 300 to 573 K, which were measured along the same direction (in-plane) as the electrical property measurement to avoid overestimating the *ZT* values. Finally, the thermal conductivity ( $\kappa$ ) was calculated using the equation  $\kappa = D \times C_p \times d$ , with the density ( $d$ ) of the sample estimated by the Archimedes method, and the specific heat ( $C_p$ ) measured by Simultaneous Thermal Analysis (STA 449F3, Netzsch, Selb, Germany). The measured  $C_p$  values, along with a comparison with the reported values, are given in Supplementary Figure S1. The longitudinal ( $v_l$ ) and transverse ( $v_s$ ) acoustic velocities were measured by an ultrasonic pulser/receiver (Ultrasonic Pulser/Receiver Model 5900 PR, Panametrics, Waltham, MA, USA). The average sound speed ( $v$ ) was then calculated by  $v^{-3} = (2v_s^{-3} + v_l^{-3})/3$ .<sup>18</sup> The thermal conductivities at low temperatures ranging from 4 to 350 K were measured using a physical property measurement system (PPMS-9T, Quantum Design, San Diego, CA, USA).

## RESULTS AND DISCUSSION

### XRD and microstructure analysis

Figure 1a presents the XRD patterns of the samples before and after texturing treatment at 633, 733 and 773 K. All the samples showed a single phase of Bi<sub>2</sub>(TeSe)<sub>3</sub>. The textured samples displayed an enhanced intensity of the (00*l*) peak and weakened intensities of the (110) and (015) peaks compared with the non-textured sample, indicating a preferred orientation along (00*l*). The degree of texturing was then determined by the orientation factors,  $F$ , using the following equations:<sup>28</sup>

$$F = \frac{P - P_0}{1 - P_0} \quad (1)$$

$$P_0 = \frac{I_0(00l)}{\sum I_0(hkl)} \quad (2)$$

$$P = \frac{I(00l)}{\sum I(hkl)} \quad (3)$$

where  $P$  and  $P_0$  are the integrated intensities of all (00*l*) planes to the intensities of all (*hkl*) planes for preferentially and randomly oriented samples. The  $F$  values of the samples before texturing and textured at 673, 733 and 773 K were 0.08, 0.38, 0.50 and 0.58, respectively, using the XRD pattern of the powder sample as a reference. The large  $F$  values obtained (0.38, 0.50 and 0.58) compared with the small value (0.08) of the non-textured sample certainly suggest a preferred crystalline orientation along (00*l*). Furthermore, the increasing  $F$  factors indicate a gradually enhanced, textured microstructure with

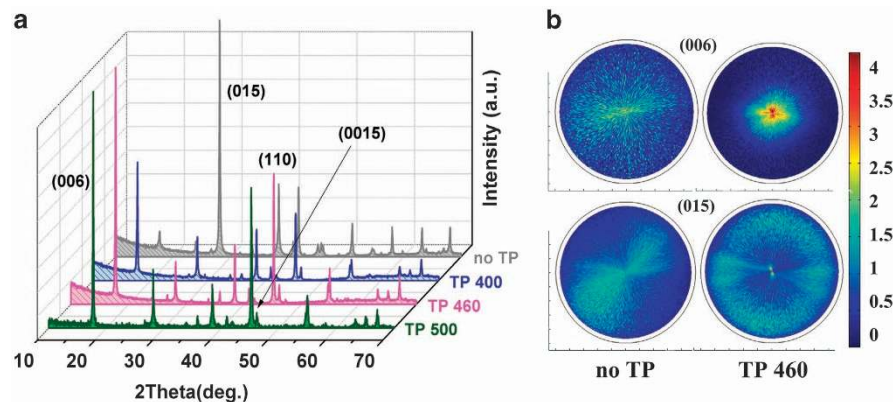


**Figure 1** (a) XRD patterns of the samples before and after the texturing treatment at different temperatures (673, 733 and 773 K). (b) (006) and (015) pole figures of non-TP and TP 460 samples.

increasing texturing temperature. Detailed studies of the textured structure were conducted by pole figures.

Figure 1b gives the pole figures of two representative crystallographic directions for samples processed under different conditions (no TP and TP 460). As shown in the upper panel, it is clear that the (006) peak intensity becomes concentrated after texturing, demonstrating a preferred orientation of (001). To confirm this situation, (015) (the strongest peak of  $\text{Bi}_2(\text{TeSe})_3$ ) pole figures were also measured, and the results are shown in the lower panel. The diffraction was more uniform before texturing, but the intensities become concentrated with a circular shape at approximately  $60^\circ$  in the textured samples, suggesting a (001)-oriented texture, which is consistent with the former results.

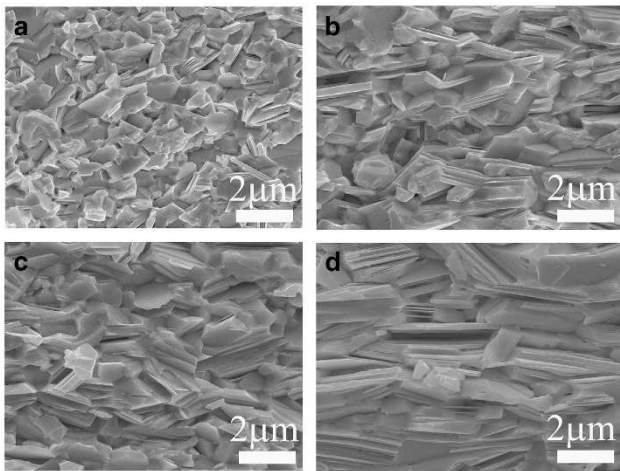


**Figure 2** SEM images of the fractured surfaces for (a) the non-textured sample and the textured samples at (b) 673 K, (c) 733 K and (d) 773 K.

The textured morphologies and the distinct influence of the processing temperature are clearly illustrated in the SEM images shown in Figure 2. As shown in Figure 2a, despite the layered structure of  $\text{Bi}_2(\text{TeSe})_3$ , it displayed a relatively isotropic microstructure with fine grain structures and a uniformly distributed porosity, when it had not been subjected to the intentionally texturing treatment. However, for the samples textured by repeated SPS, the grains clearly lengthened along the direction normal to the applied pressure, as depicted in Figures 2b–d, which was caused mainly by a crystalline plasticity slip, grain boundary sliding, grain rotation and dynamic recrystallization.<sup>29</sup> Additionally, the shape of the layered structure was enhanced with increasing texturing temperature. The samples processed at higher temperatures apparently exhibited more similar lamellar structure, which is most apparent in TP 500. Therefore, the SEM images combined with the orientation factors and pole figures confirm that the textured samples were preferentially orientated along the (001) direction, and the degree of texturing intensified with increasing texturing temperature.

### Thermoelectric properties

The electrical transport properties of the textured samples were investigated as a function of temperature, with the non-textured sample used as a reference. As shown in Figure 3a, the electrical conductivity greatly improved after the texturing treatment with the trend intensifying as the texturing temperature increased. It should be mentioned that the negative temperature dependence of the electrical conductivity, shown in Figure 3a, is indicative of semimetallic transport behavior, which is often observed in thermoelectric semiconductors. Interestingly, the absolute values of the Seebeck coefficient did not decrease but apparently increased after texturing at some temperatures, as shown in Figure 3b, although all of the textured samples exhibited higher electrical conductivities (the reasons will be discussed later). Consequently, benefiting from the simultaneous improvements of the electrical conductivity and the Seebeck

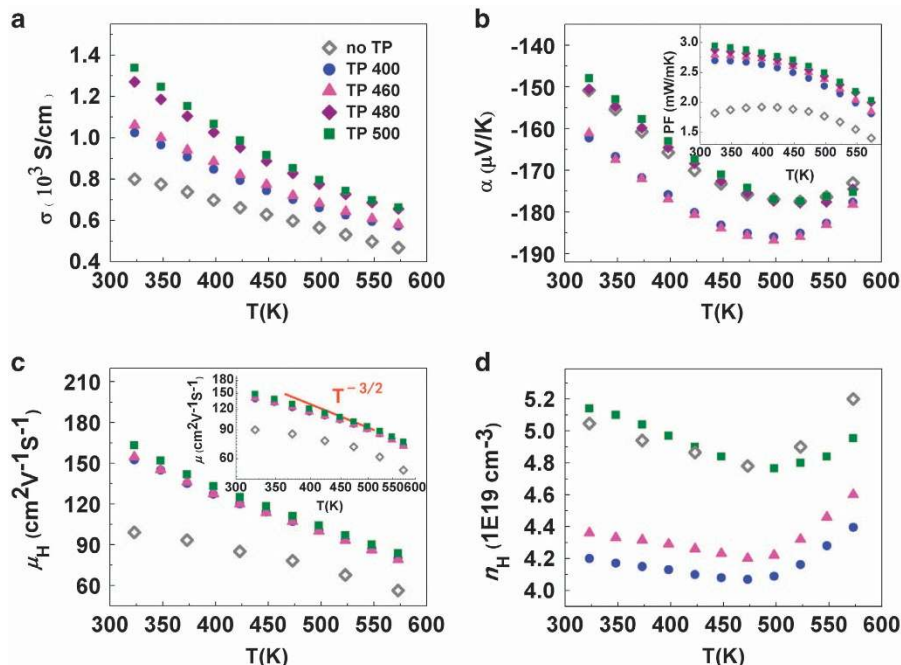


**Figure 3** The temperature dependence of the electrical transport properties: (a) the electrical conductivity, (b) the Seebeck coefficient (with an inset of the power factor), (c) the Hall carrier mobility (the inset is the  $\lg \mu \sim \lg T$  plot) and (d) the Hall carrier concentration.

coefficient, the power factors of the textured samples were remarkably enhanced as much as  $\sim 1.5$  times at room temperature, as shown in the inset of Figure 3b.

Usually, the Seebeck coefficient decreases if the electrical conductivity is enhanced. Therefore, the above results motivated us to investigate the reasons for the simultaneous increase in the electrical conductivity and the Seebeck coefficient. The Hall experiments revealed that the carrier mobility greatly increased in the textured samples and remained almost unchanged even with increasing texturing temperature, as shown in Figure 3c. The enhanced carrier mobility was associated with a high in-plane mobility as well as weakened grain boundary scattering along the textured direction. The carrier concentration showed a more interesting change after the texturing treatment, as shown in Figure 3d. At first, the carrier concentration decreased when texturing occurs at low temperatures (673 and 733 K), and it then increased at higher texturing temperature (773 K); however, it should be noted that the change in carrier concentration was limited to a small range. Therefore, it is not difficult to understand why the simultaneous enhancement of the Seebeck coefficient and electrical conductivity was realized. The electrical conductivity improved mainly because of the greatly enhanced mobility, with little influence from the carrier concentration. The increased Seebeck coefficient, especially in the TP 400 and TP 460 samples, was due to the reduced carrier concentration after texturing.

We then refocused on how the texturing temperature affected the carrier mobility and concentration. As aforementioned, samples textured at different temperatures (673–773 K) showed almost the same carrier mobilities, as displayed in Figure 3c, which is ascribed to the combined effect of the degree of texturing and the carrier concentration. When only considering the increased degree of texturing, the carrier mobility was expected to improve with increasing

texturing temperature. However, the carrier concentrations in the textured samples also increased with texturing temperature (see in Figure 3d), which suppressed any further rise in the carrier mobility. In other words, these two effects offset each other and kept the carrier mobility at a certain level.

Furthermore, a plot of  $\lg\mu$  versus  $\lg T$  at the mid-temperature range from 373 to 473 K is used to understand the electron scattering mechanism before the bipolar effect. The inset in Figure 3c shows that all of the samples roughly obey a  $T^{-3/2}$  law, revealing a dominant acoustic phonon-scattering mechanism. Here,  $\mu$  is defined from  $\mu_{\text{H}}/A$ , where  $A$  is the Hall factor, which was determined to be approximately 1.1 by the following Equation (4):

$$A = \frac{3}{4} \frac{F_{1/2} F_{-1/2}}{F_0^2}, \quad (4)$$

where  $F_j$  denotes the Fermi integration

$$F_j(\eta) = \int_0^\infty \frac{e^j d\varepsilon}{1 + \exp(\varepsilon - \eta)}. \quad (5)$$

The reduced Fermi energy  $\eta$  can be derived from the Seebeck coefficient on the basis of a single band approximation,

$$\alpha = \frac{k}{e} \left[ \frac{2F_1}{F_0} - \eta \right]. \quad (6)$$

Subsequently, the complicated behavior of the carrier concentration illustrated in Figure 3d was analyzed taking into account the point defects that strongly affected the electron density.<sup>15,19,30</sup> As mentioned above, the carrier concentration decreased when textured at low temperatures (673 and 733 K) but exhibited an increasing trend at higher texturing temperature (773 K). For  $\text{Bi}_2(\text{TeSe})_3$  polycrystals, significant attention should be paid to the donor-like effect induced from mechanical deformation:<sup>31</sup>

$$\begin{aligned} 2V_{\text{Bi}}''' + 3V_{\text{Te}}''(V_{\text{Se}}^{\bullet}) + \text{Bi}_{\text{Te}}'(\text{Bi}_{\text{Te}}') \\ = V_{\text{Bi}}''' + \text{Bi}_{\text{Bi}}^{\times} + 4V_{\text{Te}}''(V_{\text{Se}}^{\bullet}) + 6e' \end{aligned} \quad (7)$$

The above reaction was likely intensified by increases in the texturing temperature. Therefore, an increased carrier concentration with texturing temperature could result from the above reaction, which was thermally assisted. However, it is quite difficult to understand why the textured samples (TP 400 and TP 460) showed lower concentrations than the sample before texturing. Multiple reasons may exist; the microstructural changes<sup>32</sup> and the aging effect were likely influential because grain coarsening decreases the dangling bonds that donate electrons and fewer antisite defects suppress the above reaction.

As shown in Figure 4a, the total thermal conductivity obviously increased after texturing treatment and generally rose with increasing texturing temperature, with the exception of TP 460, which had the lowest values among the textured samples. Additionally, the upward trend of the thermal conductivity approximately 473 K is a result of the intrinsic excitation of minority carriers. The total thermal conductivity arises from electrical ( $\kappa_e$ ), lattice ( $\kappa_l$ ) and bipolar ( $\kappa_{\text{bipolar}}$ ) contribution. The electrical component is well described by the Wiedemann–Franz's law,  $\kappa_e = \sigma LT$ , where  $\sigma$  is the electrical conductivity,  $L$  is the Lorenz number and  $T$  is the absolute temperature. The calculated Lorenz number  $L$  is shown in Supplementary Table S1. Thus the lattice thermal conductivity was obtained using the equation  $\kappa_l + \kappa_{\text{bipolar}} = \kappa - \kappa_e$ . The lattice thermal conductivity did not correlate neatly with texturing temperature, as illustrated in Figure 4b. The uncertainty of the lattice thermal conductivity was  $\sim 5\%$ . Notably, even in consideration of the

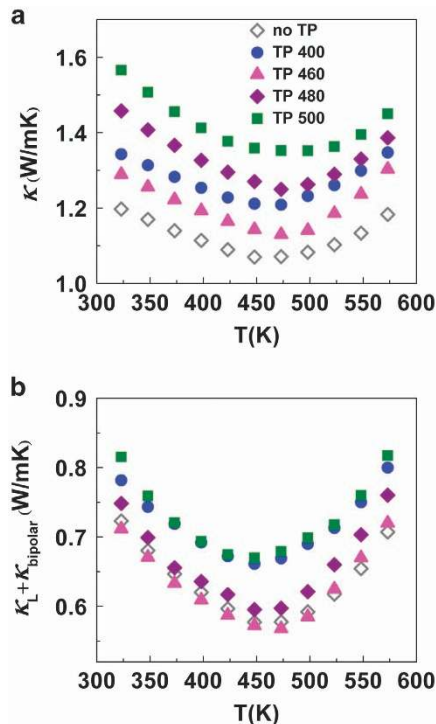


**Figure 4** The temperature dependence of the thermal transport properties: (a) the total thermal conductivity, and (b) the lattice and bipolar thermal conductivities.

uncertainty, the lattice thermal conductivity of TP 460 was still lower than those of the TP 480 and TP 500 samples, and the difference likely originates from their microstructures/nanostructures, as shown later. Samples textured at low and high temperatures (673 and 773 K) exhibited high lattice thermal conductivities with tiny differences. Intriguingly, mid-temperature (733 and 753 K) textured samples presented much lower lattice thermal conductivities, which were even comparable to the non-textured one. Indeed, the lattice thermal conductivity of TP 460 was lower than the non-TP sample. Our previous study<sup>26</sup> found that the thermal conductivity of textured Bi<sub>2</sub>Te<sub>3</sub> samples was also dependent on the texturing temperature. The reason why the lowest lattice thermal conductivity was obtained in TP 460 strongly correlates to the following finding about the texturing induced nanoscale inhomogeneity. To confirm the existence of extra phonon-scattering centers, detailed TEM observations of the textured samples were conducted.

The TEM images in Figure 5 illustrate the presence of many nanostructures with a wide size distribution in the TP 460 sample textured at 773 K. Figures 5a and b show light and dark contrast regions with a large size of ~150 nm in which a bent lattice structure and missing atoms could be seen; therefore, these regions are considered highly distorted regions. Furthermore, defect clusters as small as 10 nm were also frequently observed. Figures 5c and d clearly show the sizes of these defect clusters. In addition, the samples also contain dislocation loops and twin structures, as shown in Figures 5e–h. Notably, defects easily form in Bi<sub>2</sub>Te<sub>3</sub>-based alloys, especially when MA is applied. High-temperature heat treatment with largely mechanical deformation leads to the formation of the

nanostructured defects because of recrystallization, which has also been reported by Hu *et al.*<sup>33</sup> Low lattice thermal conductivities were associated with the nanostructures that act as phonon-scattering centers.

To clarify the specific frequency range in which the nanostructures critically target the phonons, the Callaway model was adopted, where  $\kappa_1$  is expressed as:<sup>34</sup>

$$\kappa_1(\omega) = \frac{k_B}{2\pi^2 v} \left( \frac{k_B T}{\hbar} \right)^3 \frac{z^4 e^z}{\tau^{-1} (e^z - 1)^2}. \quad (8)$$

In Equation (8),  $z = \hbar\omega/k_B T$  is the reduced phonon frequency,  $k_B$  is the Boltzmann constant,  $\hbar$  is the reduced Planck constant,  $\theta_D$  is the Debye temperature,  $v$  is the average sound velocity and  $\tau$  is the total relaxation time, which can be written as:<sup>34</sup>

$$\tau^{-1} = A\omega^4 + B\omega^2 \text{Exp}(-\theta_D/3T) + C\omega^2 + v/d. \quad (9)$$

In Equation (9),  $d$  is the grain size and  $v/d$  represents the boundary scattering and A, B and C are the preset factors for point defect scattering, Umklapp-process scattering and electron phonon scattering, respectively. For this work,  $\theta_D$  was fixed at 180 K

**Table 1** Parameters used for the Callaway model

Parameter (unit)	Value	Notes and references
Debye temperature, $\theta_D$ (K)	180	references 35,36
Sound speed, $v$ (m s <sup>-1</sup> )	1735	Measured
A (10 <sup>-40</sup> s <sup>3</sup> )	1.73	Fitted
B (10 <sup>-18</sup> s K <sup>-1</sup> )	8.88	Fitted
C (10 <sup>-16</sup> s)	1.81	Fitted

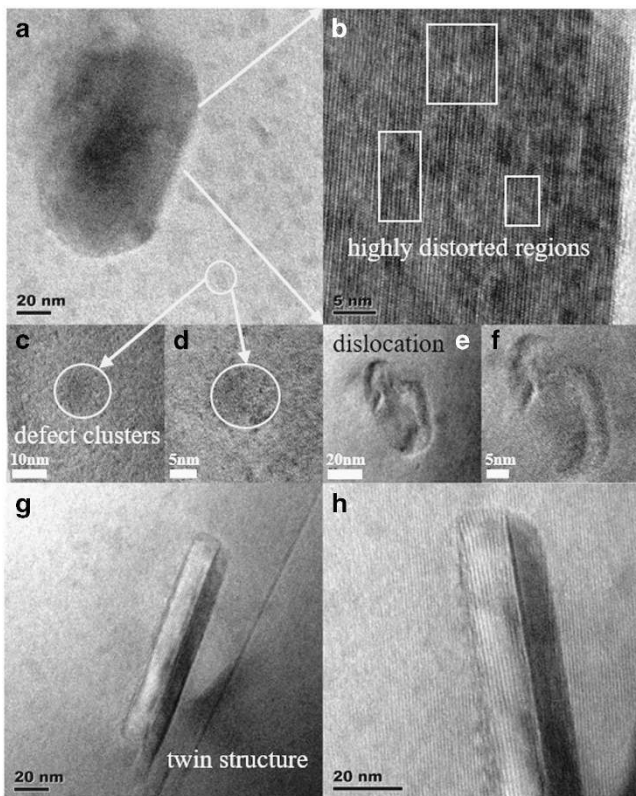


**Figure 5** TEM images of the TP 460 samples showing the lowest lattice thermal conductivity. (a, b) The highly distorted regions; (c, d) the nanoscale defect clusters; (e, f) the dislocation loops; and (g, h) twin structures.

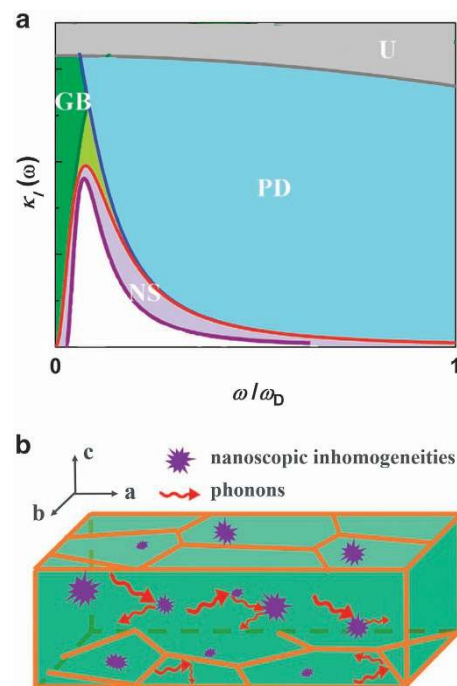


**Figure 6** (a) The contribution of nanostructures (NS) in suppressing the lattice thermal conductivity, marked with violet parts. The gray, green and blue sections are the Umklapp-process (U) scattering, the grain boundary (GB) scattering and the point defect (PD) scattering, respectively. (b) A schematic diagram of phonon scattering by nanostructures (blue dots); the red arrows present the phonon transport waves.

considering the Debye temperature of both  $\text{Bi}_2\text{Te}_3$  and  $\text{Bi}_2\text{Se}_3$ .<sup>35,36</sup> The magnitudes of A, B and C were determined via the Debye approximation, and details can be found in Supplementary Figure S2. All of the parameters are shown in Table 1.

With all of the parameters defined, one can use Equation (8) to determine the role of each scattering mechanism in suppressing the

thermal conductivity. The thermal conductivity is determined by considering the Umklapp-process, boundary scattering and point defect scattering, which are the gray, green and blue areas, respectively, as shown in Figure 6a. Because the grain boundaries decreased after texturing treatment and the alloy composition was constant, corresponding to a reduction of the green areas and the constant blue areas, respectively, the low/mid-frequency phonons were most likely to be scattered by the nanoscopic defects. Therefore, the contribution of the nanostructure-based scattering was roughly plotted in the low/mid-frequency range as the violet area under the red line (marked as NS, which is an abbreviation for nanostructures). It should be noted that, for heavily doped solid solutions (that is,  $\text{Bi}_2\text{Te}_{2.2}\text{Se}_{0.8}$  in this work), the scattering of low/mid-frequencies phonons may have a significant effect on the reduction of the lattice thermal conductivities because alloying scatters most of the high-frequency phonons.<sup>37</sup> Figure 6b further presents a schematic diagram of the scattering process. The blue dots stand for the nanostructures and the red arrows represent the phonon transport waves. Heat-carrying phonons with distinct wavelength were scattered when they encounter sizable nanoscale defects, thereby causing a decrease in the thermal conductivity.

Surprisingly, widely distributed nanoscopic defects were only found in the samples textured at high temperatures ( $> 673$  K) but not in TP 400. Figure 7a shows that the grains of TP 400 were quite clean, but defects (specified by the pink frame) were found in TP 460 and TP 500, shown as Figures 7b and c. Figure 7d presents the detailed HRTEM images of the defects in TP 500, showing a bent or distorted lattice within a small angle (circled in orange). The lower temperatures may require longer times to create a large number of defects.

As a consequence, the thermal conductivity was mainly influenced by nanoscale inhomogeneities, grain sizes and the degree of texturing, all of which clearly changed depending on the texturing temperature. Taking into account these three factors, TP 400 displayed a relatively high lattice thermal conductivity because few nanostructures existed as

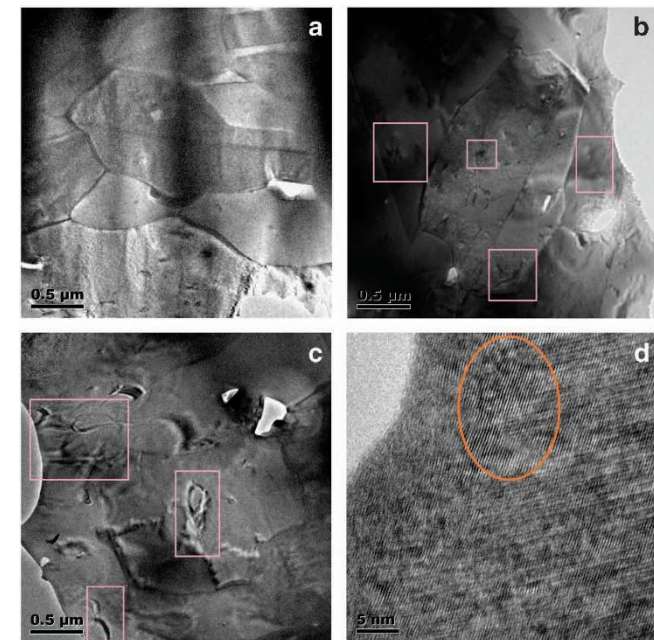


**Figure 7** TEM images of samples textured at different temperatures: (a) TP 400, (b) TP 460, and (c) TP 500. (d) HRTEM images of nanoscopic defects in TP 500.

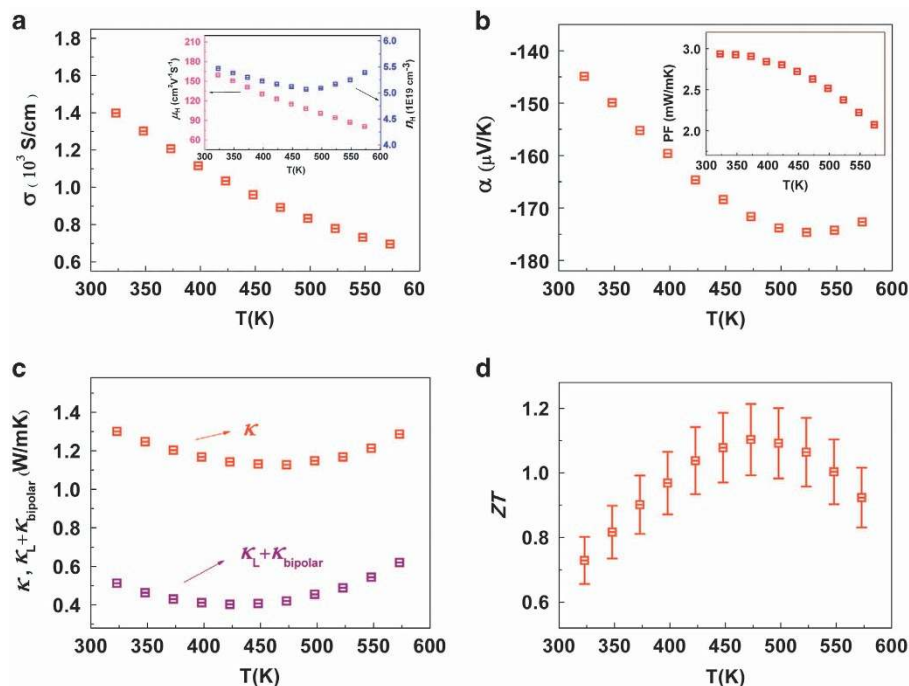


**Figure 8** The temperature dependence of the thermoelectric properties for TP 460-3. (a) Electrical conductivity, the inset is the Hall carrier mobility and carrier concentration. (b) Seebeck coefficient, the inset is power factor. (c) Total thermal conductivity and lattice thermal conductivity. (d) ZT values.

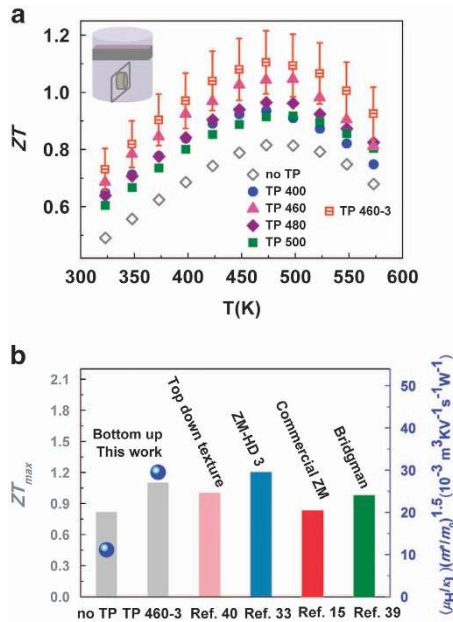


**Figure 9** (a) The temperature dependence of the  $ZT$  values and (b) the maximum  $ZT$  values (the gray columns represent this work; the other color columns are for references) and  $(\mu_H/\kappa_L)(m^*/m_0)^{3/2}$  parameters (blue dots) of the samples with different texturing conditions.

phonon-scattering centers, although with relatively fine grains. However, the high lattice thermal conductivity of TP 500 likely correlates to its highly textured structure and coarse grains. Notably, the nanoscopic inhomogeneities in TP 500 indeed limited the lattice thermal conductivity; if it had not, the lattice thermal conductivity of TP 500 would have been higher than TP 400 owing to a more textured structure and coarser grains. In contrast, the low lattice thermal conductivities of TP 460 and TP 480 were a result of the widely distributed nanoscopic inhomogeneities, medium grain sizes and moderate degree of texturing.

Because the power factors were greatly enhanced and the lattice thermal conductivity was notably reduced for TP 460, one more spark plasma texturing at 733 K was applied to TP 460, (which is referred to as TP 460-3). Figure 8 shows the detailed thermoelectric properties of TP 460-3. Remarkably, TP 460-3 exhibited an enhanced power factor and a further decrease in lattice thermal conductivity compared with TP 460, resulting in a high  $ZT$  value of 1.1 at 473 K. There are two obvious reasons for this result. First, TP 460-3 suffered again from mechanical deformation that strengthened the donor-like effect and thus increased the carrier concentration. Second, the mechanical deformation at 733 K induced more *in situ* nanoscopic defects, leading to a further decrease in the lattice thermal conductivity. This phenomenon of nano-inclusions scattering the phonons has also been reported in the melting zone of Bi<sub>2</sub>(TeSe)<sub>3</sub> alloys, for which the concept of ‘nanoparticle-in-alloy’ using a metal nanoparticle-decorated Bi<sub>2</sub>(TeSe)<sub>3</sub> alloy is adopted.<sup>38</sup>

Consequently, the  $ZT$  exceeding 1.1 for the TP 460-3 sample textured at 733 K is 35% higher than the  $ZT$  of the non-textured sample, as shown in Figure 9a. Enhanced  $ZT$  values occur for all of the textured samples compared with the non-textured one. The  $ZT$  enhancement is also remarkable when compared with commercial *n*-type Bi<sub>2</sub>(TeSe)<sub>3</sub> ingots, whose maximum  $ZT$  was measured to be  $<0.9$  in our previous work.<sup>15</sup> Although higher  $ZT$  values have been reported for *p*-type (BiSb)<sub>2</sub>Te<sub>3</sub> polycrystals, the present work has

achieved a highly improved performance of *n*-type Bi<sub>2</sub>(TeSe)<sub>3</sub> alloys, which is required for high-efficiency thermoelectric modules. Figure 9b further presents the  $ZT_{\max}$  (gray columns) as well as the parameter  $(\mu_H/\kappa_L)(m^*/m_0)^{3/2}$  (blue circles), which is proportional to the thermoelectric efficiency,<sup>14</sup> when compared with the ingots prepared by zone melting (red column)<sup>15</sup> and Bridgman methods (green column)<sup>39</sup> and with the  $ZT$  values of the textured samples.<sup>33,40</sup> Large improvements for both the  $ZT_{\max}$  and  $(\mu_H/\kappa_L)(m^*/m_0)^{3/2}$  have been achieved using a texturing treatment, and the highest  $(\mu_H/\kappa_L)(m^*/m_0)^{3/2}$  up to  $29.5 \times 10^{-3} \text{ m}^3 \text{ K V}^{-1} \text{ s}^{-1} \text{ W}^{-1}$  was obtained for the sample TP 460-3. The performance enhancement is a result of the texture-enhanced electrical transport properties, and the nanoscale defects suppressed the thermal conductivity.

Compared with work by Hu *et al.*,<sup>40</sup> in which a top-down texture method was applied to Bi<sub>2</sub>Te<sub>2</sub>Se<sub>1</sub> alloys, in this work nanoscale inhomogeneities could be introduced at appropriate temperatures to effectively decrease the lattice thermal conductivity and resulting in increased  $ZT$  values. Such temperature-controlled microstructure and nanostructure modulation is important for thermoelectric performance enhancement. Moreover, in this work we adopted spark plasma texturing with a bottom-up fabrication method to construct the multi-scale microstructures, which differs from the study by Hu *et al.*<sup>33</sup> in which zone molten ingots were repeatedly hot pressed. Because the spark plasma texturing time is much shorter than that of hot pressing, the nanostructures induced by recrystallization would be weaker, resulting in nanoscale regions with smaller areas. On the other hand, spark plasma sintering has significant features, including discharge between the sintering particles,<sup>41</sup> which might somehow affect the charged lattice defects as well as the microstructures. Moreover, in this work the optimization of the electrical and thermal performances were simultaneously realized, which was not achieved in the studies by Hu *et al.*<sup>33,40</sup>

## CONCLUSIONS

This work demonstrated the enhancement of  $ZT$  in *n*-type Bi<sub>2</sub>(TeSe)<sub>3</sub> alloys, which is required for matching the high performances of *p*-type (BiSb)<sub>2</sub>Te<sub>3</sub> alloys to manufacture high-efficiency thermoelectric devices. A significant  $ZT$  enhancement was achieved in compositionally optimized *n*-type Bi<sub>2</sub>(TeSe)<sub>3</sub> resulting in a large  $ZT_{\max} > 1.1$  at 473 K. This result was realized by simply optimizing the texturing temperature for a repeated SPS process as hot-forging. The texturing of structures greatly benefitted the electrical transport properties and led to an increase in the thermal conductivity; however, the nanostructured defects that formed during texturing at optimized temperatures could efficiently scatter low/mid-frequencies phonons, and consequently, the thermal conductivity decreased. Therefore, this work revealed the importance of combining texturing and nanostructuring techniques that can be easily realized using a spark plasma hot-forging process.

## CONFLICT OF INTEREST

The authors declare no conflict of interest.

## ACKNOWLEDGEMENTS

This work was supported by the National Basic Research Program of China (Grant No. 2013CB632503) and the National Natural Science Foundation (Nos. 11474176 and 51172121).

- 1 Bell, L. E. Cooling, heating, generating power, and recovering waste heat with thermoelectric systems. *Science* **321**, 1457–1461 (2008).
- 2 Snyder, G. J. & Toberer, E. S. Complex thermoelectric materials. *Nat. Mater.* **7**, 105–114 (2008).
- 3 Zhao, L.-D., Dravid, V. P. & Kanatzidis, M. G. The panoramic approach to high performance thermoelectrics. *Energy Environ. Sci.* **7**, 251–268 (2014).
- 4 Li, J.-F., Liu, W.-S., Zhao, L.-D. & Zhou, M. High-performance nanostructured thermoelectric materials. *NPG Asia Mater.* **2**, 152–158 (2010).
- 5 Borup, K. A., de Boor, J., Wang, H., Drymiotis, F., Gascoin, F., Shi, X., Chen, M. I., Fedorov, E., Müller, B. B., Iversen, G. J. & Snyder, X. Measuring thermoelectric transport properties of materials. *Energy Environ. Sci.* **8**, 423–435 (2015).
- 6 Zhang, X. & Zhao, L.-D. Thermoelectric materials: energy conversion between heat and electricity. *J. Materiomics* **1**, 92–105 (2015).
- 7 Qiu, W., Xi, L., Wei, P., Ke, X., Yang, J. & Zhang, W. Part-crystalline part-liquid state and rattling-like thermal damping in materials with chemical-bond hierarchy. *Proc. Natl Acad. Sci. USA* **111**, 15031–15035 (2014).
- 8 Zhao, L.-D., Lo, S.-H., Zhang, Y., Sun, H., Tan, G., Uher, C., Wolverton, C., Dravid, V. P. & Kanatzidis, M. G. Ultralow thermal conductivity and high thermoelectric figure of merit in SnSe crystals. *Nature* **508**, 373–377 (2014).
- 9 He, Y., Zhang, T., Shi, X., Wei, S.-H. & Chen, L. D. High thermoelectric performance in copper telluride. *NPG Asia Mater.* **7**, e210 (2015).
- 10 Goldsmid, H. J. Bismuth telluride and its alloys as materials for thermoelectric generation. *Materials* **7**, 2577–2592 (2014).
- 11 Hu, L.-P., Zhu, T.-J., Wang, Y.-G., Xie, H.-H., Xu, Z.-J. & Zhao, X.-B. Shifting up the optimum figure of merit of p-type bismuth telluride-based thermoelectric materials for power generation by suppressing intrinsic conduction. *NPG Asia Mater.* **6**, e88 (2014).
- 12 Poudel, B., Hao, Q., Ma, Y., Lan, Y., Minnich, A., Yu, B., Yan, X., Wang, D., Muto, A., Vashaee, D., Chen, X., Liu, J., Dresselhaus, M. S., Chen, G. & Ren, Z. High-thermoelectric performance of nanostructured bismuth antimony telluride bulk alloys. *Science* **320**, 634–638 (2008).
- 13 Kim, S. I., Lee, K. H., Mun, H. A., Kim, H. S., Hwang, S. W., Roh, J. W., Yang, D. J., Shin, W. H., Li, X. S., Lee, Y. H., Snyder, G. J. & Kim, S. W. Dense dislocation arrays embedded in grain boundaries for high-performance bulk thermoelectrics. *Science* **348**, 109–114 (2015).
- 14 Zheng, Y., Zhang, Q., Su, X., Xie, H., Shu, S., Chen, T., Gangjian, T., Yonggao, Y., Tang, X., Uher, C. & Snyder, G. J. Mechanically robust BiSbTe alloys with superior thermoelectric performance: a case study of stable hierarchical nanostructured thermoelectric materials. *Adv. Energy Mater.* **5**, 1401391 (2015).
- 15 Pan, Y., Wei, T.-R., Cao, Q. & Li, J.-F. Mechanically enhanced p- and n-type Bi<sub>2</sub>Te<sub>3</sub>-based thermoelectric materials reprocessed from commercial ingots by ball milling and spark plasma sintering. *Mater. Sci. Eng. B* **197**, 75–81 (2015).
- 16 Li, J.-F. & Liu, J. Effect of nano-SiC dispersion on thermoelectric properties of Bi<sub>2</sub>Te<sub>3</sub> polycrystals. *Phys. Stat. Sol. A* **203**, 3768–3773 (2006).
- 17 Liu, K. G., Dong, X. & Zhang, J. X. The effects of La on thermoelectric properties of La<sub>3</sub>Co<sub>4</sub>Sb<sub>12</sub> prepared by MA-SPS. *Mater. Chem. Phys.* **96**, 371–375 (2006).
- 18 Li, F., Li, J.-F., Zhao, L.-D., Xiang, K., Liu, Y., Zhang, B.-P., Lin, Y.-H., Nan, C.-W. & Zhu, H.-M. Polycrystalline BiCuSeO oxide as a potential thermoelectric material. *Energy Environ. Sci.* **5**, 7188–7195 (2012).
- 19 Hu, L., Zhu, T., Liu, X. & Zhao, X. Point defect engineering of high-performance bismuth-telluride-based thermoelectric materials. *Adv. Funct. Mater.* **24**, 5211–5218 (2014).
- 20 Yamamoto, M. & Hamada, N. First-principles estimation of Seebeck coefficient of bismuth telluride and selenide. *Jpn. J. Appl. Phys.* **51**, 125601 (2012).
- 21 Pan, Y., Wei, T.-R., Wu, C.-F. & Li, J.-F. Electrical and thermal transport properties of spark plasma sintered n-type Bi<sub>2</sub>Te<sub>3-x</sub>Se<sub>x</sub> alloys: the combined effect of point defect and Se content. *J. Mater. Chem. C* **3**, 10583–10589 (2015).
- 22 Delves, R. T., Bowley, A. E., Hazelden, D. W. & Goldsmid, H. J. Anisotropy of the electrical conductivity in bismuth telluride. *Proc. Phys. Soc.* **78**, 838–844 (1961).
- 23 Goldsmid, H. J. Recent studies of bismuth telluride and its alloys. *J. Appl. Phys.* **32**, 2198–2201 (1961).
- 24 Dennis, J. H. Anisotropy of the Seebeck coefficients of bismuth telluride. *Adv. Energy Convers.* **1**, 99–105 (1961).
- 25 Yan, X., Poudel, B., Ma, Y., Liu, W. S., Joshi, G., Wang, H., Lan, Y., Wang, D., Chen, G. & Ren, Z. F. Experimental studies on anisotropic thermoelectric properties and structures of n-type Bi<sub>2</sub>Te<sub>2.7</sub>Se<sub>0.3</sub>. *Nano Lett.* **10**, 3373–3378 (2010).
- 26 Zhao, L.-D., Zhang, B.-P., Li, J.-F., Zhang, H.-L. & Liu, W.-S. Enhanced thermoelectric and mechanical properties in textured n-type Bi<sub>2</sub>Te<sub>3</sub> prepared by spark plasma sintering. *Solid State Sci.* **10**, 651–658 (2008).
- 27 Noudem, J. G. A new process for lamellar texturing of thermoelectric Ca<sub>3</sub>Co<sub>4</sub>O<sub>9</sub> oxides by spark plasma sintering. *J. Eur. Ceram. Soc.* **29**, 2659–2663 (2009).
- 28 Lotgering, F. K. Topotactical reactions with ferrimagnetic oxides having hexagonal crystal structures—I. *J. Inorg. Nucl. Chem.* **9**, 113–123 (1959).
- 29 Bhame, S. D., Pravarthana, D., Prellier, W. & Noudem, J. G. Enhanced thermoelectric performance in spark plasma textured bulk n-type BiTe<sub>2.7</sub>Se<sub>0.3</sub> and p-type Bi<sub>0.5</sub>Sb<sub>1.5</sub>Te<sub>3</sub>. *Appl. Phys. Lett.* **102**, 211901 (2013).
- 30 Scanlon, D. O., King, P. D. C., Singh, R. P., de la Torre, A., Walker, S. M., Balakrishnan, G., Baumberger, F. & Catlow, C. R. A. Controlling bulk conductivity in topological insulators: key role of anti-site defects. *Adv. Mater.* **24**, 2154–2158 (2012).
- 31 Zhao, L. D., Zhang, B.-P., Liu, W. S., Zhang, H. L. & Li, J.-F. Effects of annealing on electrical properties of n-type Bi<sub>2</sub>Te<sub>3</sub> fabricated by mechanical alloying and spark plasma sintering. *J. Alloys Compd.* **467**, 91–97 (2009).
- 32 Wu, H., Carrete, J., Zhang, Z., Qu, Y., Shen, X., Wang, Z., Zhao, L. D. & He, J. Strong enhancement of phonon scattering through nanoscale grains in lead sulfide thermoelectrics. *NPG Asia Mater.* **6**, e108 (2014).
- 33 Hu, L., Wu, H., Zhu, T., Fu, C., He, J., Ying, P. & Zhao, X. Tuning multiscale microstructures to enhance thermoelectric performance of n-type bismuth-telluride-based solid solutions. *Adv. Energy Mater.* **5**, 1500411 (2015).
- 34 Callaway, J. Model for lattice thermal conductivity at low temperatures. *Phys. Rev.* **113**, 1046 (1959).
- 35 Shoemaker, G. E., Rayne, J. A. & Ure, R. W. Jr. Specific heat of n- and p-type Bi<sub>2</sub>Te<sub>3</sub> from 1.4 to 90 K. *Phys. Rev.* **185**, 1046 (1969).
- 36 Toher, C., Plata, J. J., Levy, O., de Jong, M., Asta, M., Nardelli, M. B. & Curtarolo, S. High-throughput computational screening of thermal conductivity, Debye temperature, and Grüneisen parameter using a quasiharmonic Debye model. *Phys. Rev. B* **90**, 174107 (2014).
- 37 Tritt, T. M. *Thermal Conductivity: Theory, Properties, and Applications* (Kluwer Academic/Plenum Publishers, New York, NY, USA, 2004).
- 38 Wang, S., Li, H., Lu, R., Zheng, G. & Tang, X. Metal nanoparticle decorated n-type Bi<sub>2</sub>Te<sub>3</sub>-based materials with enhanced thermoelectric performances. *Nanotechnology* **24**, 285702 (2013).
- 39 Yim, W. M. & Rosi, F. D. Compound tellurides and their alloys for peltier cooling—a review. *Solid-State Electron.* **15**, 1121–1140 (1972).
- 40 Hu, L. P., Liu, X. H., Xie, H. H., Shen, J. J., Zhu, T. J. & Zhao, X. B. Improving thermoelectric properties of n-type bismuth-telluride-based alloys by deformation-induced lattice defects and texture enhancement. *Acta Mater.* **60**, 4431–4437 (2012).
- 41 Anselmi-Tamburinia, U., Gennari, S., Garay, J. E. & Munir, Z. A. Fundamental investigations on the spark plasma sintering/synthesis process: II. Modeling of current and temperature distributions. *Mater. Sci. Eng. A* **394**, 139–148 (2005).



This work is licensed under a Creative Commons Attribution 4.0 International License. The images or other third party material in this article are included in the article's Creative Commons license, unless indicated otherwise in the credit line; if the material is not included under the Creative Commons license, users will need to obtain permission from the license holder to reproduce the material. To view a copy of this license, visit <http://creativecommons.org/licenses/by/4.0/>

Supplementary Information accompanies the paper on the NPG Asia Materials website (<http://www.nature.com/am>)